Materials Horizons

ROYAL SOCIETY OF CHEMISTRY

COMMUNICATION

View Article Online
View Journal | View Issue

Cite this: *Mater. Horiz.*, 2026, 13, 786

Received 18th June 2025,
Accepted 22nd October 2025

DOI: 10.1039/d5mh01167a

rsc.li/materials-horizons

Bimetallic organic cages as precise theranostic nanoplatforms for self-enhanced magnetic resonance imaging and chemodynamic therapy

Yucen Deng,†[ab] Xin Fang,†[b] Yingfang Lv,†[c] Xinyuan Zhu,[b] Youfu Wang,*[b] Xiaoyan Wang*[c] and Xuesong Feng*[a]

Chemodynamic therapy (CDT) faces efficiency and safety challenges due to glutathione (GSH) overexpression in the tumor microenvironment (TME) and the lack of therapeutic feedback. In this study, a ferrocene (Fc) decorated metal organic cage (MOC-Fc) was constructed through coordination self-assembly between Fc-based ligands and copper ions, and its bimetallic synergistic and oxidation-responsive feature enables the theranostic integration of self-enhanced CDT and magnetic resonance imaging (MRI). The obtained MOC-Fc possesses an atomically precise cage-like structure with uniformly ultrasmall size. *In vitro* experiments demonstrated that MOC-Fc could effectively catalyze the Fenton-like reaction and significantly enhance the ROS-induced cell death through bimetal mediated GSH depletion. Concurrently, the MOC-Fc exhibited exceptionally T_1-weighted MRI capabilities due to the TME responsive states of the bimetal ions. In a nude mouse model of subcutaneous pancreatic cancer implantation, MOC-Fc successfully achieved MRI of the tumor and significantly inhibited its growth without significant systemic toxicity. This work proposes a novel paradigm for the development of precise, highly efficient, and visualized CDT nanoplatforms, and its catalytic-imaging bifunctional integration strategy establishes a theoretical foundation for the precision treatment of tumors and clinical translation.

New concepts

Chemodynamic therapy (CDT) struggles with limited efficacy and safety concerns caused by excessive glutathione (GSH) in tumors and the absence of real-time treatment monitoring. A ferrocene-decorated metal–organic cage (MOC-Fc) was designed through coordination self-assembly to address CDT challenges, combining bimetallic synergy and oxidation-responsiveness for self-enhanced CDT and MRI. The ultrasmall MOC-Fc structure efficiently catalyzes Fenton-like reactions and enhances ROS-mediated cell death by depleting GSH in the tumor microenvironment. It also enables T_1-weighted MRI due to bimetallic ion responsiveness, allowing real-time tumor visualization. *In vivo* studies demonstrated effective tumor growth inhibition and MRI capability without systemic toxicity, offering a promising theranostic platform for precise CDT.

1. Introduction

Cancer poses a significant threat to global public health, with the World Health Organization (WHO) reporting over 20 million new cancer cases and nearly 10 million deaths worldwide in 2022 alone.[1–3] While conventional therapeutic modalities such as surgery, chemotherapy, and radiotherapy remain clinical standards, they suffer from considerable limitations including systemic toxicity, non-specific distribution, and development of treatment resistance.[4] In recent years, metal-based nanoparticles (NPs) have emerged as promising theranostic platforms due to their unique physicochemical properties and multifunctional capabilities.[5–8] These metal-based NPs play essential roles in biological processes and can be engineered to respond to the tumor microenvironment (TME).[9–11] Their versatility enables applications in catalytic therapy, drug delivery, and biomedical imaging, making them ideal candidates for developing integrated theranostic platforms.[12–17] As extensively reviewed in recent literature, transition metal-based NPs offer unprecedented opportunities for precision medicine due to their tunable structures and diverse biological activities. In particular, iron- and copper-based NPs have garnered significant attention for cancer diagnosis and therapy.

Capitalizing on these merits, chemodynamic therapy (CDT) has gained prominence as a compelling anticancer approach that harnesses intrinsic characteristics of the tumor microenvironment (TME), including its mild acidity and elevated hydrogen peroxide (H_2O_2) levels. In contrast to conventional

[a] School of Pharmacy, China Medical University, Shenyang 110122, P. R. China. E-mail: xsfeng@cmu.edu.cn
[b] School of Chemistry and Chemical Engineering, State Key Laboratory of Polyolefins and Catalysis, Research Institute of Polymer Materials, Shanghai Jiao Tong University, Shanghai 200240, P. R. China. E-mail: wyfown@sjtu.edu.cn
[c] Shanghai Center for Systems Biomedicine, Shanghai Jiao Tong University, Shanghai 200240, P. R. China. E-mail: cathywxy@sjtu.edu.cn
† These authors contributed equally to this work.

treatments, CDT employs metal-based catalysts (*e.g.*, Fe^{2+} and Cu^{+}) that trigger Fenton or Fenton-like reactions, leading to the *in situ* generation of highly toxic hydroxyl radicals ($^{\bullet}OH$). These radicals provoke oxidative damage to key biomolecules, resulting in selective cancer cell death while preserving healthy tissues. Furthermore, the strategic design of multi-metal systems capitalizes on synergistic interactions between different metallic elements, thereby enhancing the therapeutic performance of CDT agents. Despite these strengths, conventional CDT nanoplatforms still confront several limitations: (1) the abundant glutathione (GSH) present in the TME can scavenge the generated reactive oxygen species (ROS), thereby diminishing treatment outcomes; (2) the catalytic activity and self-regeneration capacity of single-metal agents remain insufficient; and (3) real-time monitoring of therapeutic progress is generally unfeasible, hindering timely feedback.[18] Consequently, the creation of multifunctional theranostic nanoplatforms that can simultaneously counteract GSH depletion and facilitate diagnostic imaging is essential for advancing CDT toward clinical translation.

Ferrocene (Fc), a classical organometallic compound, exhibits distinctive redox activity and biocompatibility, attributable to its stable 'sandwich' structure. In recent years, the application of Fc in CDT has gradually gained attention.[19–21] Firstly, the Fc molecule contains iron ions, which can effectively catalyze the Fenton/Fenton-like reaction in a weakly acidic TME. Secondly, hydrophobic cyclopentadienyl moieties have shown enhanced cell membrane penetration of the nanocarriers. Finally, the Fe^{2+}/Fe^{3+} redox pair in the Fc molecule can complete the cycle from the oxidation to reduction state by consuming GSH, and its cycling stability is superior to that of traditional iron-based catalysts, which is conducive to enhancing the CDT effect.[22,23] However, the majority of current Fc-based (nano)agents focus on the catalytic function of a single metal, failing to make full use of the synergistic effect of multi-metals and lacking diagnostic and therapeutic integration design. The ambiguous structure of current CDT-based nano-agents also presents significant challenges in understanding their structure–activity relationship, ensuring quality control, and facilitating clinical translation.

As emerging nanoobjects with atomically precise structures and multi-component features, metal organic cages (MOCs) formed through the coordination-driven self-assembly of metal nodes and organic ligands exhibit unique advantages in nanomedicine due to their well-defined structures, programmable topology, and dynamic responsiveness.[24–26] These features enable three critical functionalities: (1) the intrinsic catalytic activity of metal nodes (*e.g.*, iron and copper) provides endogenous therapeutic capabilities, such as ROS generation for CDT and ROS clearance for anti-inflammation. (2) Surface functionalization or modification facilitates targeted delivery and stimuli-responsive release, optimizing spatiotemporal control over therapeutic action. (3) The cavity confinement effect allows efficient encapsulation of therapeutic drugs or catalytic molecules, enhancing payload stability and delivery precision.[27–29] Despite these merits, existing MOC designs predominantly focus on single therapeutic modalities, failing to integrate diagnostic functionalities. Leveraging the diverse physicochemical and catalytic properties of transition metals, the rational design of multimetal MOCs holds significant promise for advancing theranostic platforms that synergistically integrate diagnostic imaging, targeted therapy, and real-time therapeutic monitoring.[30]

To achieve these goals, this study developed a Fc-based MOC (MOC-Fc) that integrates therapeutic and diagnostic functions through a bimetal synergistic strategy. By leveraging Fc-functional ligand self-assembly with copper ions, the obtained MOC-Fc as a precise theranostic nanoplatform combines the CDT effect of Fc with the MRI capability of copper ions, while exploiting the redox activity of bimetallic response to the TME to amplify both therapeutic and imaging performance (Scheme 1). Under simulated TME conditions, MOC-Fc establishes a self-sustaining catalytic cycle: continuous $^{\bullet}OH$ production *via* the Fenton-like reaction is coupled with Cu^{2+}- and Fe^{3+}-mediated GSH depletion, overcoming the limitations of traditional CDT. Simultaneously, the cavity confinement effect of MOCs accelerates the electron transfer between Fc and copper ions, significantly boosting Fenton-like reaction kinetics for sustained $^{\bullet}OH$ generation. Specifically, the T_1-weighted MRI capability of paramagnetic copper ions is enhanced by the TME responsive oxidation state of Fc from pure Fe^{2+} to partial Fe^{3+} during the CDT process. Experimental validation demonstrated superior cancer cell killing efficacy and MRI signal amplification, attributed to the synergistic interplay of bimetallic active centers. *In vitro* and *in vivo* studies confirmed the system's biocompatibility, tumor-targeting efficiency, and real-time visualization of therapeutic progression, achieving a "diagnosis-treatment-monitoring" triad. This work not only advances the design of bimetallic MOC-based nanosystems but also provides a paradigm for integrating catalytic enhancement, diagnostic precision, and therapeutic adaptability in next-generation nanomedicine.

2. Results and discussion

2.1. Synthesis and characterization of MOC-Fc

Through the coordination between copper ions and the isophthalic acid moiety within the ligand, MOC and MOC-Fc can be efficiently formed (Fig. 1A and B). The OEG moiety within the ligand provides water solubility, while the Fc moiety and copper ions provide self-enhanced Fenton-like activity and a responsive MRI signal. The detailed synthesis and characterization of the ligands and MOCs are available in the SI (Scheme S1 and Fig. S1–S10). To confirm the successful synthesis of MOC-Fc, the ^{1}H NMR spectra of L-Fc and MOC-Fc were compared. The signals from MOC-Fc exhibit significant chemical shifts to lower fields and peak broadening compared to those of the ligand alone (Fig. S7 and S10). For example, the chemical shifts of the two hydrogens on the benzene ring in L-Fc were 8.18 and 6.72 ppm, respectively, which changed to 8.62 and 7.20 ppm in MOC-Fc. The broadening and merging of peaks indicate the successful synthesis of MOC-Fc.[31] Additionally, MALDI-TOF-MS was used to measure the molecular weights of MOC and MOC-Fc (Fig. 1C). The theoretical molecular weights of MOC and MOC-Fc were 16 060 g mol^{-1} and

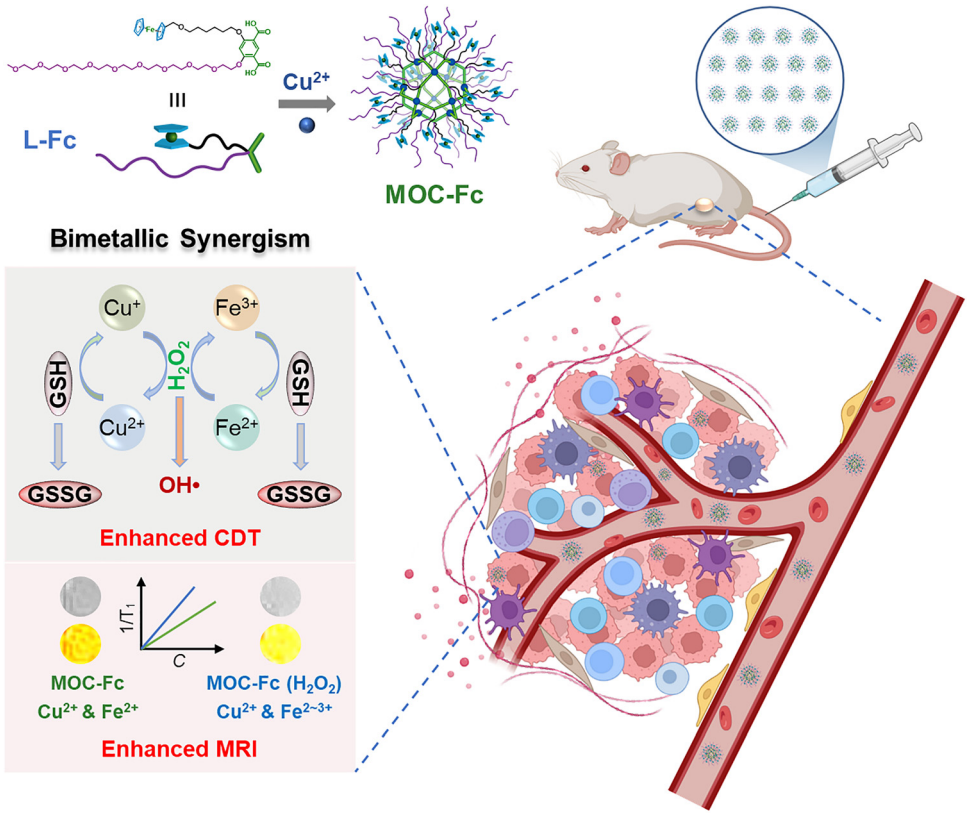

Scheme 1 The atomically precise MOC-Fc with bimetallic activity as a theranostic nanoplatform for self-enhanced CDT and MRI for cancer treatment.

23 215 g mol^{-1}, respectively.[32] The observed peaks in the spectra of MOC and MOC-Fc (16 060 and 23 289 g mol^{-1}) matched well with these theoretical values, confirming the successful synthesis of MOC and MOC-Fc with a cuboctahedral structure and $Cu_{24}L_{24}$ or $Cu_{24}(L\text{-}Fc)_{24}$ formula.

FT-IR was used for further structural characterization of the MOCs (Fig. 1D). Notably, both ligands and MOCs share characteristic signal peaks, reflecting their structural similarities. For instance, both ligands exhibit a carboxylic acid signal at 1721 cm^{-1}, which is absent in MOCs and MOC-Fc due to the coordination effect.[32] The stretching vibrational peak of the Fe–O bond in Fc appeared at 625 cm^{-1}, but this peak was not observed in the L and MOC spectra. These findings confirm the successful coordination of the ligands and the formation of the MOCs. XPS curve (Fig. 1E) showed that MOC-Fc contains C, O, Fe, and Cu, with respective contents of 58.4%, 28.3%, 7.07%, and 6.19%, consistent with theoretical results of 54.57%, 26.43%, 5.77%, and 6.56%. High-resolution analysis of Cu 2p revealed clear spin–orbit splitting characteristics and satellite peaks at approximately 943 eV (Fig. S11), indicating that Cu 2p ions are stabilized in the divalent form within MOC-Fc. High-resolution analysis of Fe 2p also revealed a satellite peak at approximately 708.0 and 720.7 eV (Fig. S11), indicating the stable presence of ferrocene containing divalent iron ions within MOC-Fc. These further support the hypothesis that L-Fc was effectively coordinated with Cu^{2+} to form the structurally stable MOC-Fc.

SEC is a highly efficient separation technique suitable for characterizing macromolecular homologues with similar chemical properties but different molecular size distributions. Given the substantial molecular weights of MOC and MOC-Fc, SEC was employed to analyze their molecular weight, stability, and polydispersity (Fig. 1F). Both L and L-Fc exhibited single sharp peaks at 22.08 min and 20.93 min, respectively, while MOC and MOC-Fc showed single sharp peaks at 20.20 min and 18.76 min, respectively. The shorter elution times for MOC and MOC-Fc suggest their larger hydrodynamic volumes. The molecular weights of MOC and MOC-Fc, as determined from the SEC plots, were 15 763 g mol^{-1} and 22 976 g mol^{-1}, respectively, closely matching the above-mentioned theoretical values. The polydispersity indices (PDIs) derived from the experimental analyses were 1.02 and 1.07, indicating excellent homogeneity, discreteness, and stability of both MOCs.

After confirming the successful synthesis of MOC-Fc, its size and morphology were investigated using atomic force microscopy (AFM) (Fig. 1G). The height of MOC-Fc was approximately 6.5 nm, consistent with the theoretical size of cuboctahedral MOCs reported in the literature. The AFM images also revealed a high degree of homogeneity, confirming the structural stability and uniformity of MOC-Fc. Transmission electron microscopy (TEM) was further used to observe the morphology and size of MOC-Fc, revealing its nearly spherical structure and uniform, ultrasmall size of approximately 7 nm (Fig. S12).

The surface modification of the OEG portion of MOC-Fc renders it amphiphilic, providing a distinct safety advantage

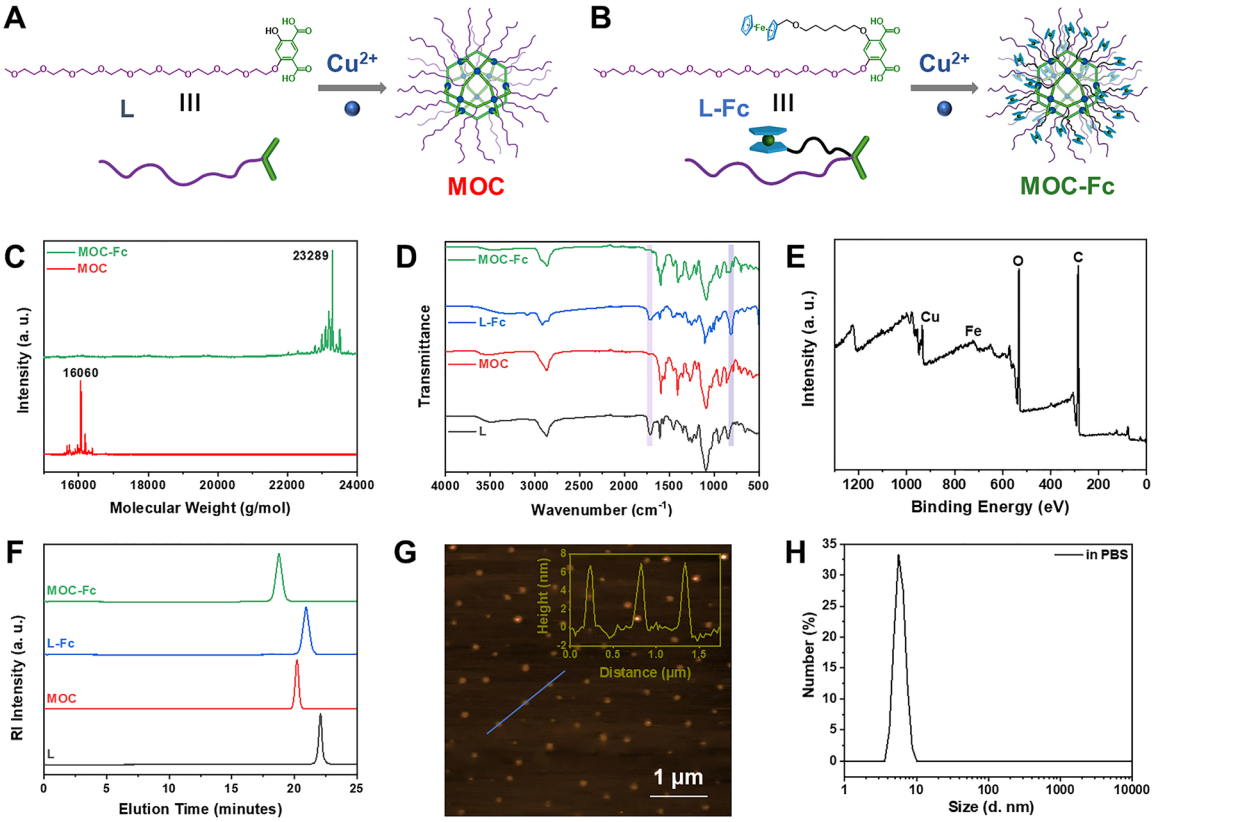

Fig. 1 Structures and characterization of MOCs. (A) and (B) Structures of ligands, MOC, and MOC-Fc. (C) MALDI-TOF MS spectra of MOC and MOC-Fc. (D) The FT-IR spectra of ligands, MOC, and MOC-Fc. (E) The XPS curve of MOC-Fc. (F) SEC profile of ligands, MOC, and MOC-Fc. (G) The AFM image and height analysis of MOC-Fc. Scar bar: 1 μm. (H) DLS plot of MOC-Fc in PBS.

over other nanoplatforms, which are often limited to solubility in organic solvents for biological applications.[33] To evaluate the suitability of MOC-Fc for biological applications, we measured its particle size and zeta potential. The hydrated particle size of MOC-Fc was approximately 7.0 nm, and no significant changes were observed in the DLS results after dissolution in H_2O over one day and in FBS or TME-mimic conditions over six days (Fig. 1H and Fig. S13), indicating its stable structure. The zeta potential of MOC-Fc (Fig. S14) showed a slightly negative charge of approximately −0.9 mV, making it relatively safe for use in biological systems.

2.2. Fenton-like activity and GSH scavenging capacity in solution

To verify the activity of MOC-Fc, UV-Vis spectroscopy was utilized due to its high sensitivity and the spectral range of ligands and MOCs does not affect subsequent testing (Fig. S15). To verify the Fenton-like activity of the synthesized MOC-Fc, we detected the generation of hydroxyl radicals during the reaction between MOC-Fc and H_2O_2 using the TMB colorimetric method with UV-Vis spectroscopy. The peak resulting from oxidized TMB by hydroxyl radicals appeared near 652 nm, and its absorbance increased over time as oxidation progressed.[34,35] Firstly, we compared the catalytic activities of L-Fc, MOC, and MOC-Fc (Fig. 2A). The characteristic peak did not appear in the PBS group but increased significantly in both the L-Fc and MOC-Fc groups, indicating their effective catalytic generation of hydroxyl radicals. MOC-Fc demonstrated stronger catalytic activity than L-Fc, attributed to its cuboctahedral structure, which can accommodate more Fc active components at the same concentration, thereby catalyzing the Fenton reaction more efficiently. Notably, the MOC group exhibited a weak absorbance at 652 nm, suggesting a minor catalytic activity, possibly due to Cu^{2+} involvement in the coordination. However, this activity was negligible compared to MOC-Fc, so we did not investigate it further. The Fenton activity of MOC-Fc exhibited time-dependent and concentration-dependent behaviors. The absorbance showed a continuous increase with time (Fig. 2B) and concentration (Fig. S16), indicating the continuous generation of hydroxyl radicals. The kinetic behavior of MOC-Fc was also evaluated using TMB in an acidic environment (Fig. S17). The results show that MOC Fc has good performance with a V_{max} of 0.26 μM s^{-1} and a K_m of 161 μg mL^{-1}.

The catalytic activity of MOC-Fc in the Fenton reaction was further evaluated by EPR spectroscopy at different pH (Fig. 2C and D).[36,37] It is evident that the characteristic signal peaks of hydroxyl radicals (1 : 2 : 2 : 1) do not appear in the MOC group, indicating that the hydroxyl radicals are catalytically generated by the Fc-active moieties in MOC-Fc. Additionally, MOC-Fc exhibited superior catalytic performance in acidic environments (pH 6.5) compared to neutral conditions (pH 7.4), generating a significant amount of hydroxyl radicals within 5

min, suggesting its potential to efficiently catalyze the Fenton reaction in the weakly acidic TME.

Given that the current CDT systems face key bottlenecks, such as the high concentration of GSH in the TME, which can neutralize ROS and weaken therapeutic effects, developing multifunctional nanoplatforms capable of efficient GSH scavenging is crucial for advancing the clinical translation of CDT.[38–44] To verify that MOC-Fc enhances CDT efficacy by depleting GSH, we examined its GSH scavenging ability using DTNB. DTNB reacts with the sulfhydryl group of GSH to produce yellow 5-thio-2-nitrobenzoic acid, which has a maximum absorption peak at 412 nm. As GSH content decreases, absorption at 412 nm decreases. We first compared the GSH scavenging abilities of L-Fc, MOC, and MOC-Fc (Fig. 2E). The experimental results revealed distinct GSH scavenging capacities among the materials: L-Fc demonstrated limited scavenging activity, whereas MOC exhibited significantly enhanced efficacy due to its copper-mediated GSH consumption mechanism. Notably, MOC-Fc integrating Fc moieties and copper ions achieved optimal GSH depletion through a synergistic bimetallic interaction. This enhanced performance can be attributed to a sequential redox cycling process. Initially, Cu^{2+} ions actively oxidize GSH while undergoing reduction to Cu^{+}. Concurrently, Fe^{2+} undergoes oxidation to Fe^{3+}, which subsequently participates in GSH consumption through its reduction back to Fe^{2+}. This coordinated redox cycling between copper and iron species establishes a catalytic cascade that amplifies GSH depletion efficiency, as the two metal centers mutually regenerate their active oxidation states while continuously consuming the cellular antioxidant. We also assessed the GSH scavenging ability of MOC-Fc at different concentrations (Fig. S18) and over time (Fig. 2F). The absorption at 412 nm decreased with increasing concentration and time, indicating continuous consumption of GSH in the system, even at relatively low concentrations of MOC-Fc.

Due to the potential of Fenton-like activity of Cu^{+}, this activity of reduced Cu^{+} within MOC or MOF-Fc during GSH scavenging was also investigated using MB as a hydroxyl radical indicator with a UV-vis absorption peak at 660 nm. When hydroxyl radicals react with MB, they reduce it to colorless leuco-MB, resulting in a decrease in absorbance.[45] We set up six

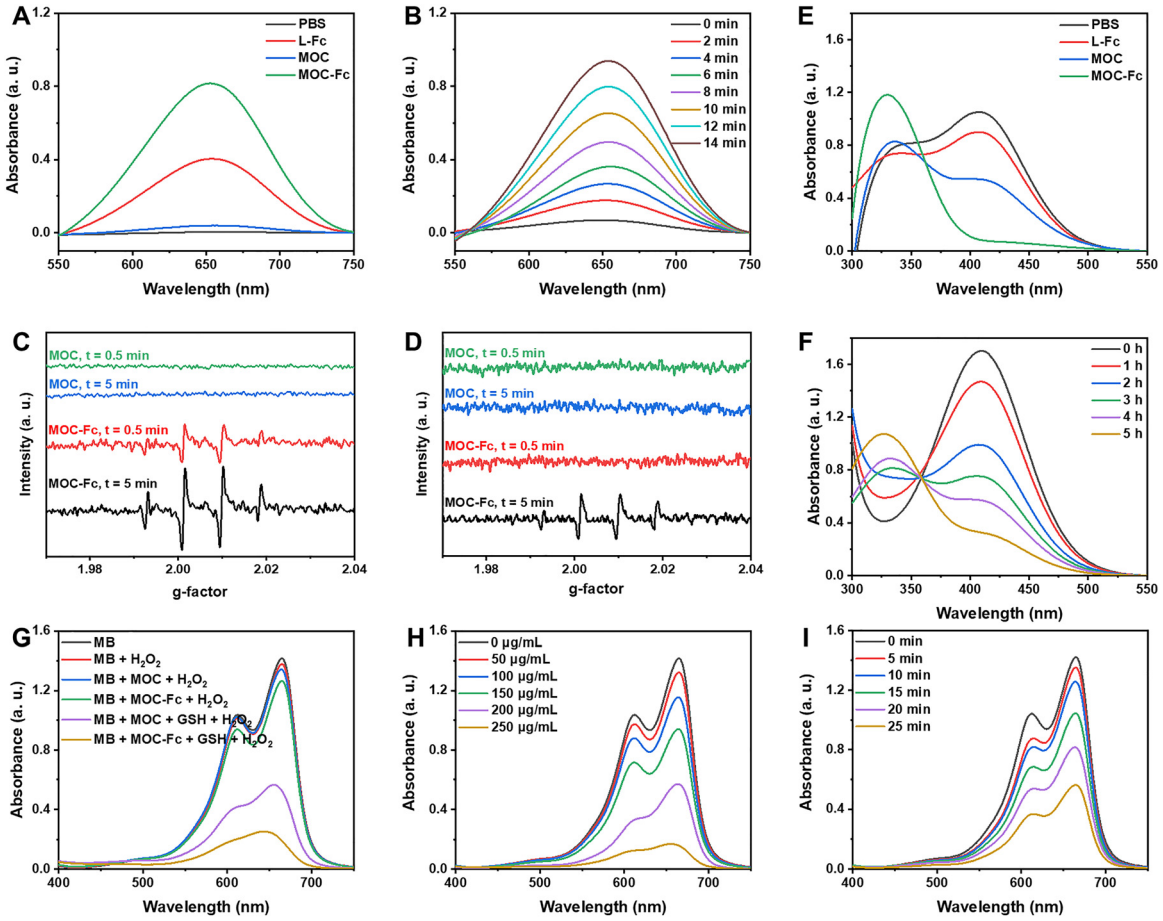

Fig. 2 Fenton-like activity and GSH scavenging capacity of MOC-Fc. (A) Comparative Fenton-like activity of L-Fc, MOC, and MOC-Fc using the TMB colorimetric method. (B) Fenton-like activity of MOC-Fc using TMB as a detector over time. (C) and (D) Comparative Fenton-like activity of MOC and MOC-Fc using the EPR method at pH 6.5 (C) and 7.4 (D). (E) Comparison of GSH scavenging abilities of L-Fc, MOC, and MOC-Fc by DTNB. (F) The GSH scavenging ability of MOC-Fc over time. (G) Comparative CDT effects of different groups by MB in the presence of GSH. (H) and (I) The CDT effect of MOC-Fc by MB at different concentrations or different time of MOC-Fc in the presence of GSH.

groups containing MB and controlled variables, obtaining the corresponding UV-vis spectra (Fig. 2G). The absorption in the groups with added GSH and MOCs and H_2O_2 significantly decreased, confirming our hypothesis that Cu^+ reduced during GSH scavenging also catalyzes the Fenton reaction to generate hydroxyl radicals. Additionally, the MOC-Fc group showed the largest change in MB absorbance, suggesting that Fe^{2+} also contributes to hydroxyl radical generation. The GSH scavenging exhibited concentration- and time-dependent behavior (Fig. 2H and I). In summary, MOC-Fc can enhance hydroxyl radical generation while scavenging GSH, thereby promoting the effects of CDT.

2.3. *In vitro* MRI

The potential of MRI to provide high-quality, non-invasive images of tissues and organs has revolutionized modern medicine, leading to more accurate diagnoses and more effective treatments while reducing the risks associated with invasive procedures. To investigate the diagnostic and therapeutic potential of MOC-Fc, the imaging capabilities and longitudinal relaxation rate (r_1) of L-Fc, MOC, and MOC-Fc in aqueous solutions were quantified using a 0.5T MRI scanner. It was determined that both MOCs have favorable relaxation rates, which are attributed to the paramagnetism of Cu^{2+} and Fe in the structure. Among them, the r_1 value of MOC-Fc was 8.25 mM^{-1} s^{-1} (Fig. 3A), higher than that of L-Fc treated with H_2O_2, MOC, MOC treated with H_2O_2, indicating the pivotal role of copper ions in the imaging process. It is noteworthy that the H_2O_2 treatment resulted in a substantial enhancement in the r_1 values of both MOC-Fc and L-Fc. Given the inherent difficulty to oxidize Cu^{2+} and almost no change before and after H_2O_2 treatment of MOC, this suggests the potential for Fe^{2+} in MOC-Fc to be converted into Fe^{3+} through an oxidative response, thereby facilitating MRI signal enhancement with a high r_1 value to 12.36 mM^{-1} s^{-1}. We also compared MOC-Fc with clinically used MRI contrast agents (*e.g.* Gd-DTPA). As summarized in Table S1, MOC-Fc showed significantly higher relaxivity than Gd-DTPA and other agents, highlighting its enhanced contrast capability.

Subsequently, a comparison was made of the T_1-weighted MRI signal intensities of the samples (Fig. 3B). The findings indicated that the addition of H_2O_2 led to an enhancement in signal intensity for the MOC-Fc group, surpassing that of the MOC group. This observation corroborated our hypothesis that MOC-Fc could potentiate MRI by amplifying magnetic resonance capacity through an oxidative response, thereby enhancing the MRI effect. Furthermore, an increase in the concentration of MOC-Fc led to enhanced image contrast and relaxation, suggesting that its imaging performance is concentration-dependent. Furthermore, previous studies have demonstrated that paramagnetic transition metals substantially enhance relaxation; however, their cardiotoxicity restricts their application.[46–49] In contrast, MOC-Fc stabilizes metal ions, thereby reducing toxicity while maintaining optimal imaging performance. These findings emphasize the considerable potential of MOC-Fc as a T_1 contrast agent for diagnostic applications and lay the foundation for further research.[50]

2.4. *In vitro* Fenton-like activity and GSH scavenging capacity

A preliminary assessment of the biosafety of MOC-Fc was conducted to evaluate its hemolytic potential *in vitro*. This assessment utilized extracted erythrocytes as a model system. The results indicated that MOC-Fc exhibits excellent biosafety in blood contact scenarios, even at the higher concentration tested (250 μg mL^{-1}), the hemolysis rate was below the safety threshold of 5% (Fig. S19).[51] Additionally, an analysis of the metal elements in MOC-Fc using ICP-MS was performed to investigate the internalization capacity of MOC-Fc in human pancreatic cancer cells (Capan-1) (Fig. 4A). The results showed that the intracellular uptake of MOC-Fc was about 347.5 μg/10^6 cells after 12 h. The intracellular content of MOC-Fc after 8 h of removal of free MOC-Fc was about 217.9 μg/10^6 cells and the calculated retention rate was more than 60%.

The MTT assay was used to assess the cytotoxic effects of MOC-Fc on normal cells (hTERT-HPNE) (Fig. S20).[52,53] Within the concentration range of 0–150 μg mL^{-1}, the cell survival rate remained above 85% in all groups, indicating good biocompatibility. The cytotoxicity of MOC-Fc on cancer cells (Capan-1) was also evaluated, providing preliminary verification of its CDT effect (Fig. 4B). As the concentration increased, the cell survival rates in both the L-Fc and MOC-Fc groups exhibited a

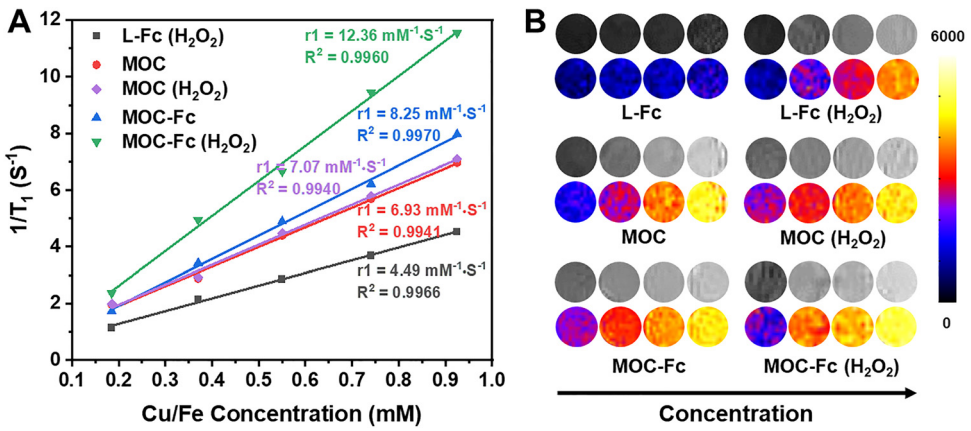

Fig. 3 *In vitro* MRI property of MOC-Fc. (A) r_1 of related samples. (B) The *in vitro* MRI image of L-Fc, MOC, and MOC-Fc before and after oxidation treatment with concentrations of 0.37, 0.55, 0.73, and 0.92 mM, respectively.

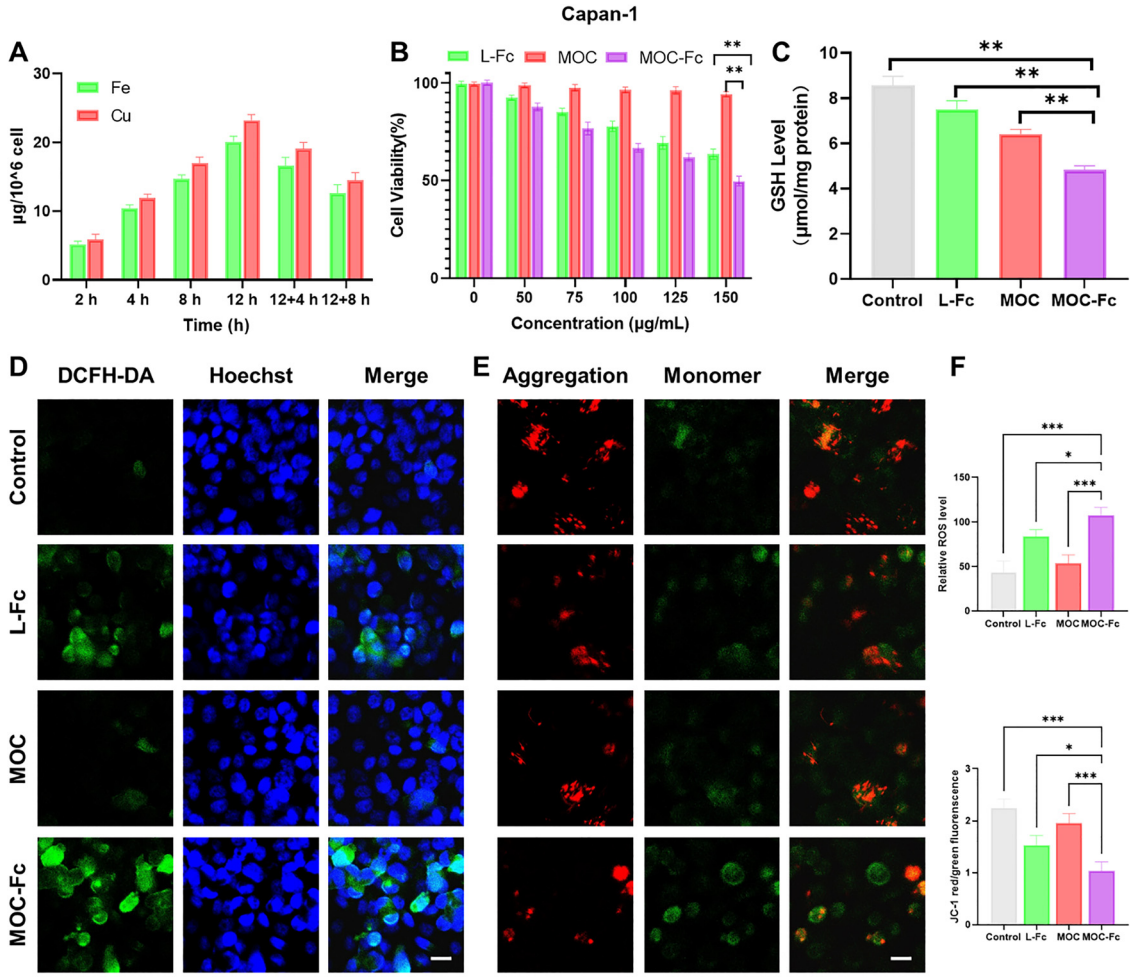

Fig. 4 *In vitro* Fenton-like activity and GSH scavenging capacity of MOC-Fc. (A) Cellular uptake and retention of MOC-Fc in Capan-1 cells. (B) The *in vitro* toxicity of L-Fc, MOC, and MOC-Fc in Capan-1 cells. (C) GSH depletion of L-Fc, MOC, and MOC-Fc in Capan-1 cells. (D) ROS images in Capan-1 cells treated with different groups. (E) JC-1 staining images in Capan-1 cells treated with different groups. (F) Quantitative results of D and E. Scale bar: 10 μm. Data are presented as mean ± SD (n = 6). *P < 0.05, **P < 0.01, and ***P < 0.001.

significant decrease. The IC_{50} value of MOC-Fc was determined to be approximately 149.34 μg mL^{-1}, fully demonstrating the biocompatibility of MOC-Fc as a CDT agent.

To elucidate the regulatory impact of MOC-Fc on the endogenous antioxidant system of tumor cells, a systematic detection of GSH levels in Capan-1 cells was conducted using the DTNB assay (Fig. 4C). After 24 h of treatment with 150 μg mL^{-1} MOC-Fc, the intracellular GSH content decreased to 4.7 ± 0.3 μmol mg^{-1} protein, representing a 44.7% reduction compared to the blank control group, which had 8.5 ± 0.5 μmol mg^{-1} protein. This finding suggests substantial GSH depletion. Integrating these results with previous studies, we hypothesize that MOC-Fc induces GSH depletion through a dual pathway: firstly, the Fenton reaction initiated by MOC-Fc produces Fe^{3+}, which accelerates GSH depletion ($2Fe^{3+} + 2GSH \rightarrow 2Fe^{2+} + GSSG + 2H^{+}$); secondly, Cu^{2+} within MOC-Fc directly oxidizes GSH, forming oxidized glutathione (GSSG), further exacerbating depletion.

To comprehensively evaluate the capacity of MOC-Fc to catalyze ROS generation at the cellular level, an assay using a ROS detection kit was conducted (Fig. 4D and F).[54] The results showed that the green fluorescent signal, indicative of ROS, was strongest in the MOC-Fc group, suggesting its superior ability to generate ROS. Furthermore, the apoptosis of Capan-1 cells was examined using the JC-1 kit (Fig. 4E and F).[55] A lower ratio of red to green fluorescence signals indicated a higher degree of apoptosis. Treatment with L-Fc and MOC-Fc significantly reduced the ratio of JC-1 aggregates (red fluorescence signals) to JC-1 monomers (green fluorescence signals), while no significant differences were observed in other groups. These findings suggest that the Fenton reaction, catalyzed by the ferrocene active ingredient, promotes ROS accumulation, leading to increased apoptosis. Compared to L-Fc, MOC-Fc demonstrated a substantial reduction in mitochondrial membrane potential in cellular models, indicating its enhanced capacity to induce apoptosis in Capan-1 cells. This further substantiates its remarkable CDT effect.

2.5. *In vivo* anticancer and MRI capacity

To further confirm the anticancer effects of MOC-Fc at the Murine model level, its biocompatibility was initially evaluated. The major organs of the mice were collected and stained with hematoxylin and

eosin (H&E) 24 h after drug administration. The results (Fig. S21) demonstrated that none of the organs exhibited significant tissue damage, indicating that L-Fc, MOC, and MOC-Fc were biocompatible and did not produce tissue toxicity at the administered dose.

Subsequently, to validate the efficacy of MOC-Fc in treating tumors *in vivo*, we conducted experiments on tumor-bearing mice. The initial administration of MOC-Fc was initiated when the tumor volume reached approximately 90–100 mm^3. This administration was repeated every two days, and the mice were euthanized on day 14. During this period, the mice were continuously monitored for changes in body weight (Fig. 5A). The results revealed no statistically significant variations in

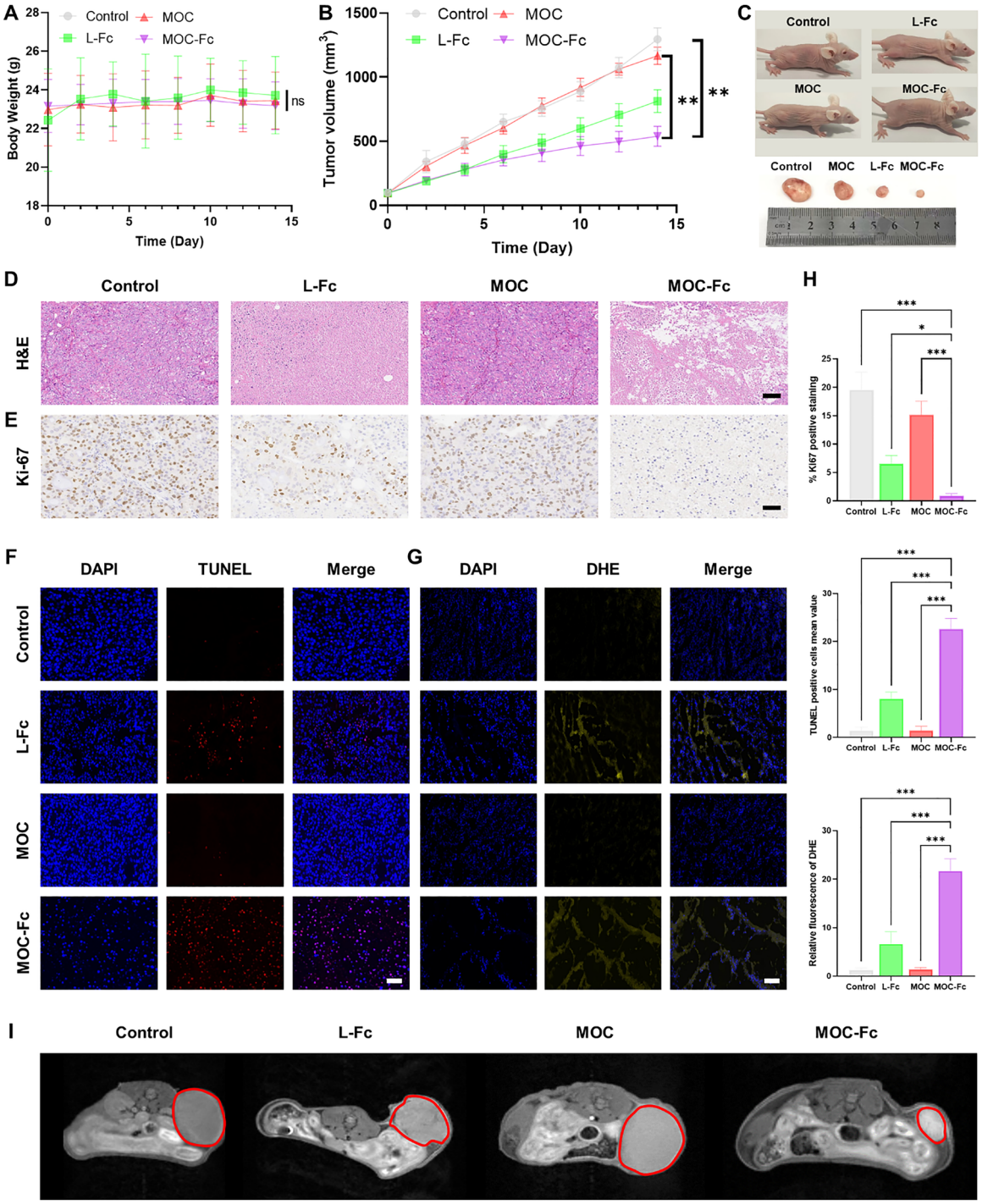

Fig. 5 *In vivo* CDT and MRI of MOC-Fc. (A) Body weight and (B) tumor volume changes in Capan-1 tumor-bearing mice after different treatments for 14 days. (C) Representative tumor-bearing mice and isolated tumor tissue under different treatments. (D) H&E, (E) Ki-67, (F) TUNEL, (G) DHE staining images of tumors after 14 days of treatment. Scale bar: 50 μm. Data are presented as mean ± SD (n = 5). *P < 0.05, **P < 0.01, and ***P < 0.001. (H) Quantitative results of E, F and G. (I) *In vivo* MRI of tumor-bearing mice under different treatments.

body weight within each group throughout the study, suggesting that none of the materials exhibited significant toxicity. The study also included the analysis of tumor growth (Fig. 5B). Compared to the control group, the tumor volume of mice treated with MOC showed minimal changes. Conversely, the tumor inhibition rate in the L-Fc group was approximately 37.1%, while the tumor inhibition rate in the MOC-Fc group was approximately 57.6%, indicating the most effective anti-tumor growth effect. Additionally, while the L-Fc group exhibited an initial inhibitory effect on tumor growth, it did not maintain a sustained inhibitory effect comparable to that observed in the MOC-Fc group over the experimental period. This difference can be attributed to the pharmacokinetics of L-Fc, a small molecule that is rapidly cleared by the body following administration. The representative tumor growth conditions in different groups were illustrated (Fig. 5C). The MOC-Fc group exhibited superior tumor inhibitory activity compared to the other groups.

To understand the fate of MOC-Fc after administration to tumor-bearing mice, we quantified the MOC-Fc content in various organs and tissues using ICP-MS to detect the elemental Cu content (Fig. S22). The accumulation of MOC-Fc in mice peaked around 12 h after tail vein injection, with relatively high levels detected in tumor tissues.

Tumor tissues were then collected and analyzed to visually assess the tumor suppression effect of each group. H&E staining revealed that the MOC-Fc group exhibited the most significant degree of tissue damage, characterized by substantial necrotic areas in the center, accompanied by apoptosis (Fig. 5D). The results of the Ki-67 proliferation marker assay demonstrated that the percentage of Ki-67-positive cells was significantly lower in the MOC-Fc group compared to the other groups. The ki-67 proliferation inhibition rates of L-Fc, MOC, and MOC-Fc are 66.53%, 22.34%, and 95.46%, respectively (Fig. 5E and H), suggesting that MOC-Fc effectively impedes the proliferative capacity of tumor cells. Furthermore, the TUNEL assay showed that the MOC-Fc group demonstrated the most pronounced apoptosis in treated tumors. The induced apoptosis rates of L-Fc, MOC and MOC-Fc were determined to be 8.10%, 1.43% and 22.57%, respectively (Fig. 5F and H). The results of the serum biochemical analysis showed that all tested parameters were within normal limits. These findings collectively indicate a lack of significant side effects from MOC and MOC-Fc and suggest their good biocompatibility (Fig. S23). Collectively, these findings indicate that MOC-Fc exerts its antitumor effects through a dual mechanism involving the inhibition of proliferation and the promotion of apoptosis.[56]

Additionally, DHE staining was used to detect the ROS content in tumor tissues (Fig. 5G and H). The fluorescence intensity in the MOC-Fc group was significantly enhanced, indicating that MOC-Fc could induce a substantial amount of ROS in tumor tissues, thereby demonstrating its exceptional CDT properties.

We also performed a T_1-weighted MRI assay on tumor-bearing mice using a small-animal MRI system to explore the diagnostic ability of MOC-Fc for cancer (Fig. 5I). The signal intensity in the tumor region was low in the control group, while both MOC groups showed some intensity. The administration of the L-Fc group significantly enhanced the T_1-MR contrast in the tumor margin region. Prior studies have shown that Fe^{3+}, obtained from the oxidation of Fe^{2+} in ferrocene, enhances T_1-weighted imaging signals in MRI. Therefore, it can be hypothesized that the catalytic property of the Fenton reaction is activated by the TME when L-Fc enters the tumor *via* the bloodstream, generating ROS and large amounts of Fe^{3+}, which further enhances the T_1-weighted imaging signals at the tumor edge. This phenomenon may also explain the enhanced imaging signal observed for MOC-Fc compared to MOC. Furthermore, the oxidized Fe^{3+} state is predicted to further enhance MRI performance. By carefully regulating the coordination environment of copper ions, the cage structure not only stabilizes the relaxation properties of copper ions but also prevents their non-specific binding with biomolecules, ensuring the reliability of the imaging signals. A comprehensive evaluation of the *in vitro* MRI results in tumor-bearing mice revealed that MOC-Fc exhibited favorable T_1-MRI performance at the biological level. This finding suggests that MOC-Fc could play a crucial role in facilitating comprehensive tumor diagnosis and treatment strategies.

3. Conclusion

In summary, this study successfully developed a precisely bimetallic theranostic nanoplatform, MOC-Fc, which synergizes enhanced CDT and MRI through Fe/Cu dual-metal synergy. By integrating Fc with copper ions into MOC-Fc, the system achieves atomically precise nanostructures with ultrasmall size, enabling TME-responsive self-enhanced catalytic and imaging functionalities. The self-sustaining catalytic cycle—driven by Fe^{2+}/Fe^{3+}- and Cu^{2+}/Cu^{+}-mediated Fenton-like reactions and GSH depletion—overcomes limitations of traditional CDT, such as antioxidant resistance and insufficient ROS generation. Concurrently, oxidation-state transitions of Fe and Cu ions enhance T_1-weighted MRI contrast, enabling real-time visualization of tumor loci and therapeutic progression. This work bridges diagnostic precision with therapeutic action, addressing the "blind therapy" challenge of conventional CDT and establishing a paradigm for adaptive, image-guided nanomedicine. This work also establishes a blueprint for next-generation nanomedicine, showcasing how multimetal MOC architectures can integrate therapeutic, diagnostic, and adaptive functionalities. The platform's scalability, biocompatibility, and clinical-grade imaging compatibility position it as a viable candidate for precision oncology. Future efforts will explore stimulus-responsive ligand engineering for multimodal imaging and combinatorial therapies.

4. Experimental

4.1. Materials

All chemicals and solvents were commercially available and did not require further purification. 2,5,8,11,14,17,20,23,26-Neoxacosan-28-ol, dimethyl 4,6-dihydroxyisophthalate, ferrocenylmethanol, 6-bromo-1-hexanol, copper acetate monohydrate,

lithium hydroxide, glutathione (GSH), 5,5-dimethyl-1-pyrroline N-oxide (DMPO), 3,3′,5,5′-tetramethylbenzidine (TMB), 5,5′-disulfanediylbis(2-nitrobenzoic acid) (DTNB), and methylene blue (MB) were obtained from Bide Pharmatech Co., Ltd (China). Sodium hydroxide, *p*-toluenesulfonyl chloride, tetrahydrofuran, dichloromethane, ethyl acetate, triethylamine, sodium chloride, anhydrous magnesium sulfate, silica gel, cesium carbonate, *N*,*N*-dimethylformamide, methanol, glacial acetic acid, and dimethylsulfoxide were sourced from Shanghai Titan Scientific Co., Ltd (China). Hydrochloric acid and nitric acid were purchased from Sinopharm Chemical Reagent Co., Ltd (China).

Trypsin cell digest (0.25% trypsin), MTT Cell Proliferation and Cytotoxicity Assay Kit, Mitochondrial Membrane Potential Assay Kit (JC-1), Reactive Oxygen Demonstration Kit, Cell lysis buffer for Western and IP, GSH and GSSG assay kits, Human Pancreatic Cancer Cells (Capan-1), Human Normal Pancreatic Ductal Cells (hTERT-HPNE) and Penicillin–Streptomycin Solution (100X) were obtained from Beyotime Biotech. Inc. (China). PBS was purchased from Wuhan Servicebio Technology CO., Ltd (China). Fetal Bovine Serum (FBS), Iscove's modified Dulbecco's medium (IMDM), and Dulbecco's Modified Eagle's Medium (DMEM) were purchased from GIBCO BRL (USA).

4.2. Synthesis and characterization

The synthetic details of ligands and MOCs are provided in the SI. The structures of the synthesized compounds were preferentially confirmed by nuclear magnetic resonance (NMR) spectroscopy on a Bruker Avance 500 (500 MHz) instrument. Their precise molecular weights were determined by mass spectrometry (MS), quadrupole time-of-flight LC/MS mass spectrometry on a Bruker Impact II (Bruker, Germany) and matrix-assisted laser desorption ionization time-of-flight (MALDI-TOF) mass spectrometry on a Bruker Speed MALDI-TOF 7090 (Bruker, Germany). The molecular weights and polydispersity indices (PDIs) of the ligands and MOCs were also determined by size exclusion chromatography (SEC). The SEC was carried out using poly(methyl methacrylate) as a standard with THF as the eluent at a flow rate of 1.0 mL min^{-1} at 35 °C. The FT-IR spectra were recorded using a Bruker Tensor 27 FT-IR spectrometer, with the samples undergoing ATR measurements. The particle size and zeta potential analyzer in the ZS90 instrument was utilized primarily for the study of particle size, size distribution and surface charge. An Oxford MFP-3D Atomic Force Microscope (AFM) was utilized to characterize the surface morphology and size of the MOC-Fc. A Bruker A300 Electron Paramagnetic Resonance (EPR) instrument was utilized to study the nature of hydroxyl radicals. An ESCALAB Qxi type X-ray Photoelectron Spectrometer (XPS) was employed to measure the elemental spectra. An inductively coupled plasma mass spectrometer (ICP-MS) (i CAP Q, Thermo) was used to detect cellular uptake and tissue distribution. The UV-Vis spectra were recorded on a UV-2600i (Shimadzu) instrument, and a MesoMR23-060H-I low-field MRI analyzer was used to measure relaxation rates and to study *in vitro* MRI. Finally, the BioSpec 94/30 USR Small Animal MRI System was used to study *in vivo* MRI in small animals.

4.3. Detection of hydroxyl radicals using TMB as an indicator

TMB was employed as an indicator to detect the generation of hydroxyl radicals in Fenton or Fenton-like processes. The characteristic absorption peak of oxidized TMB by hydroxyl radicals is located near 652 nm. This absorbance gradually increases with the extent of oxidation, thereby reflecting the production of hydroxyl radicals indirectly. To monitor this process, the absorbance at 652 nm in the UV-Vis spectra of oxidized TMB was observed.

Firstly, the ability of four samples to generate hydroxyl radicals under identical experimental conditions was investigated: PBS (50 μL), L-Fc (2 mg mL^{-1}, 50 μL), MOC (2 mg mL^{-1}, 50 μL), and MOC-Fc (2 mg mL^{-1}, 50 μL) were added to the mixture of TMB (12 mg mL^{-1}, 50 μL), H_2O_2 (0.4 mol L^{-1}, 50 μL), and acetate buffer (pH 3.6, 2 mL), then mixed thoroughly for 12 min, and analyzed. Then, time and concentration gradients of MOC-Fc were established to examine its catalytic efficiency in generating hydroxyl radicals from H_2O_2. Specifically, TMB (12 mg mL^{-1}, 50 μL), MOC-Fc (2 mg mL^{-1}, 50 μL), and H_2O_2 (0.4 mol L^{-1}, 50 μL) were added to acetate buffer (pH 3.6, 2 mL), mixed thoroughly, and then analyzed. The UV-Vis absorption spectra were recorded every 2 min. Subsequently, the catalytic effect of MOC-Fc at various concentrations (0–175 μg mL^{-1}) was further explored.

4.4. Detection of hydroxyl radicals using EPR spectrum

In this study, DMPO was used as a trapping agent for hydroxyl radicals. DMPO solution (100 mM, 50 μL) and H_2O_2 solution (5 mM, 50 μL) were prepared separately using ultrapure water, and mixed with MOC or MOC-Fc (2 mg mL^{-1}, 50 μL) at different pH (6.5 and 7.4). Temporal variation of hydroxyl radical generation was then investigated.

4.5. Detection of GSH consumption capacity and CDT enhancement capacity by DTNB

The consumption of GSH was investigated using DTNB as an indicator through UV-Vis spectroscopy. The substance generated by the reaction between DTNB and GSH has a maximum absorption peak at 412 nm, and by detecting the absorption peak, the change of GSH content in the system can be reflected. In this study, four samples were prepared to compare the GSH scavenging ability: PBS, L-Fc, MOC and MOC-Fc. The sample solutions (1 mg mL^{-1}, 0.25 mL) were mixed with GSH solution (1 mg mL^{-1}, 0.5 mL), H_2O_2 solution (5 mM, 0.5 mL), purified water (1 mL), and PBS buffer (pH 6.5, 0.5 mL) and incubated in an oven at 37 °C for 30 min under light protection. After incubation, DTNB solution (3 mg mL^{-1}, 0.2 mL) was added immediately and mixed well, followed by the assay. Then, the GSH scavenging effect of different concentrations of MOC-Fc (0-125 μg mL^{-1}) and the changes over time (0–5 h) were also evaluated under the same conditions.

Additionally, MB was also used as an indicator to detect the generation of hydroxyl radicals during the consumption of GSH by MOC-Fc, with the characteristic peak located at 660 nm. Six samples were set up to detect the generation of hydroxyl

radicals during the consumption process: MB, MB + H_2O_2, MB + MOC + H_2O_2, MB + MOC-Fc + H_2O_2, MB + MOC + GSH + H_2O_2, and MB + MOC-Fc + GSH + H_2O_2. The concentration of the MB solution was 0.5 mg mL^{-1}, the H_2O_2 solution was 5 mM, the MOC or MOC-Fc solution was 1 mg mL^{-1}, and the GSH solution was 1 mg mL^{-1}. The samples of each group were mixed thoroughly and then incubated at 37 °C for 30 min, protected from light, and the absorbance was measured. Then, time and concentration gradients of MOC-Fc were established under the same conditions.

4.6. *In vitro* MRI detection

The metal ion (Cu or Fe) concentration gradients of the samples in the study were controlled at 0.18, 0.37, 0.55, 0.74, and 0.92 mmol L^{-1}. The longitudinal relaxation rates (r_1) of L-Fc, MOC, and MOC-Fc were initially evaluated in the T_1-weighted mode at these concentrations. Furthermore, the alterations in relaxation rates of these three samples following oxidation treatment by H_2O_2 solution (1 mmol L^{-1}) and 1% HCl solution were further compared.

Finally, 1 mL of the above sample solutions with different concentrations (0.2, 0.4, 0.6, and 0.8 mmol L^{-1} of Cu or Fe) of each group was placed in a 1.5 mL centrifuge tube for T_1-weighted sequence imaging. The differences in the imaging performance of L-Fc, MOC, MOC-Fc, and related oxidized samples were quantitatively assessed and compared by signal intensity.

4.7. Hemolysis

Fresh whole blood (0.3 mL) from healthy mice was placed in a 2 mL EP tube containing an anticoagulant. The blood was centrifuged (2500 rpm, 5 min) to isolate the red blood cells, which were then washed three times with PBS and diluted to a 5% red blood cell suspension. Different concentrations of MOC-Fc solution (0.5 mL) were added, with PBS and DDW water serving as negative and positive controls, respectively. The solutions were mixed well and incubated at 37 °C for 2 h. Pictures were taken to record the experimental results.

4.8. Cell uptake and retention

Capan-1 cells (10 000 cells per mL, 200 μL) were divided into six groups and inoculated into 96-well plates. The cells were cultured for 24 h to allow adherence. Subsequently, MOC-Fc (150 μg mL^{-1}, 10 μL) was added to each group for co-incubation. After 2, 4, 8, and 12 h of incubation, the cells were digested with trypsin and collected by centrifugation. For the other two groups, the original culture medium was discarded after 12 h of incubation, and the cells were washed with PBS and replaced with fresh medium. After 4 and 8 h, the cells were collected. The collected cells were digested in a mixture of HCl (37%, 0.75 mL) and HNO_3 (68%, 0.25 mL) at 120 °C for 2 h. After cooling to room temperature, the samples were diluted to 10 mL with HCl (2%) and analyzed by ICP-MS for Fe and Cu contents.

4.9. Cytotoxicity assay

The cytotoxic effects of MOC-Fc on Capan-1 and hTERT-HPNE cells were evaluated using a commercial MTT kit. Capan-1 and hTERT-HPNE cells were inoculated in 96-well plates at 7000 cells per well and incubated with MOC-Fc at different concentrations (0–150 μg mL^{-1}, 10 μL) for 24 h. The medium was discarded, and the wells were washed gently with PBS three times. MTT working solution was added to each well, and the incubation continued for 4 h at 37 °C. After the incubation, the MTT working solution was discarded, and 100 μL of DMSO was added to each well. The plate was shaken gently for 10 min to dissolve the purple formazan completely. Absorbances at 570 nm were measured using an enzyme meter.

4.10. GSH depletion assay

The GSH depletion effect of MOC-Fc in cancer cells was assessed using a GSH assay kit (Biotronik S0053). Capan-1 cells treated with MOC-Fc, MOC, or L-Fc for 12 h were washed three times with pre-cooled PBS, lysed on ice with cell lysis solution for 30 min, and the supernatant was collected by centrifugation at 10 000 rpm for 15 min at 4 °C. 50 μL of each sample was mixed with an equal volume of DTNB working solution in a 96-well plate and incubated at 37 °C for 30 min under light protection. The absorbances were measured at 412 nm using an enzyme counter. GSH concentrations were calculated using a standard curve (0–100 μM GSH gradient). Untreated cells and cell-free blanks were included to eliminate background interference.

4.11. *In vitro* ROS generation assay

An *in vivo* assay for ROS generation was conducted to evaluate the capacity of MOC-Fc to produce ROS in cells. This assay utilized a ROS assay kit (DCFH-DA). Capan-1 cells in the logarithmic phase of growth were digested with trypsin, collected by centrifugation (2000 rpm, 3 min), and inoculated in laser confocal dishes at a concentration of 2.5×10^6 cells per mL. After 24 h of incubation to allow cell adhesion, MOC-Fc, L-Fc, or MOC (150 μg mL^{-1}, 10 μL) was co-incubated with the cells for 12 h. The cells were washed three times with PBS, and DCFH-DA solution (10 μmol mL^{-1}, 150 μL) and Hoechst 33342 solution (10 μg mL^{-1}, 150 μL) were added to the culture dish and incubated at 37 °C for 20 min. After discarding the solution, the cells were washed three times with PBS to remove unincorporated fluorescent dye. Fluorescence distribution was observed under a confocal microscope.

4.12. Apoptosis assay

The mitochondrial membrane potential assay kit (JC-1) was used to evaluate the capacity of MOC-Fc to induce apoptosis. Capan-1 cells in the logarithmic phase of growth were digested with trypsin, collected by centrifugation (2000 rpm, 3 min), and inoculated into laser confocal dishes at a concentration of 2.5×10^6 cells per mL. After 24 h of incubation to allow cell adhesion, MOC-Fc, L-Fc, or MOC (150 μg mL^{-1}, 10 μL) was co-incubated with the cells for 12 h. The cells were washed three times with PBS, and JC-1 working buffer (150 μL) and Hoechst 33342 solution (10 μg mL^{-1}, 150 μL) were added to the dish and incubated at 37 °C for 20 min. After discarding the contents, the cells were washed twice with JC-1 staining buffer (1X) to remove

unincorporated fluorescent dye. JC-1 fluorescence distribution was observed under a laser confocal microscope.

4.13. *In vivo* safety experiments

To evaluate the biocompatibility of L-Fc, MOC, and MOC-Fc materials, BALB/c mice were administered with these materials *via* tail vein injection (150 μg mL^{-1}, 100 μL/each). The animals were euthanized 12 h after injection, and the heart, liver, spleen, lungs, and kidneys were rapidly removed and fixed in 4% paraformaldehyde solution for 24 h at room temperature. The tissues were then dehydrated with gradient ethanol, made transparent with xylene, and embedded in paraffin. Serial sections of 4 μm thickness were prepared with a microtome, stained with hematoxylin–eosin (H&E), and examined by light microscopy for pathological changes in the major organs.

4.14. Animal tumor model

BALB/c nude mice (female, 4–5 weeks old) were purchased from the Shanghai Laboratory Animal Center (China). All animal experiments were conducted in accordance with the Guide for the Care and Use of Laboratory Animals of the National Institute of Health (NIH) and approved by the Scientific Investigation Committee of Shanghai Jiao Tong University (No. 202501013). Capan-1 cells were cultured and observed under a microscope. When the cells reached 90–95% confluence, the medium was discarded, and the cells were washed with PBS three times. The cells were digested with trypsin (0.25%), and the digestion was stopped by adding IMDM complete medium after 2–3 min. The cells were centrifuged at 1500 rpm for 3 min, resuspended in PBS, and counted. Capan-1 cells (5×10^7 cells per mL, 100 μL) were inoculated into the right thigh of the mice to establish a xenograft tumor model. The mice were divided into four groups of five mice each: PBS, L-Fc, MOC, and MOC-Fc. Tumor size was assessed daily using vernier calipers, and the tumor volume (mm^3) was calculated. Drug administration began when the tumor volume reached 90–100 mm^3. Each group received a single dose (150 μg mL^{-1}, 100 μL) *via* the caudal vein every 2 days, with a total of four doses administered.

4.15. *In vivo* MR imaging

One BALB/c mouse from each group was randomly selected and given of sample solution (150 μg mL^{-1}, 100 μL/each) *via* tail vein injection. 60 min after injection, the mice were anesthetized with isoflurane and scanned using a coronal T_1-weighted sequence on a 9.4 T small animal MRI system.

4.16. *In vivo* distribution study

The distribution of MOC-Fc in major organs and tissues was quantitatively analyzed using ICP-MS. The MOC-Fc solution (150 μg mL^{-1}, 100 μL) was injected into the tumor-molded mice *via* the tail vein, and the mice were euthanized at the designated time. Blood and the heart, liver, spleen, lungs, kidneys, and tumor tissues were obtained, weighed, and placed in a solution containing HNO_3 (68%, 0.25 mL) and HCl (37%, 0.75 mL) at 100 °C for 6 h. After cooling, the samples were diluted to 10 mL with HCl (2%), and the elemental Cu content was determined by ICP-MS.

4.17. Histopathological evaluation of tumors

Two weeks after the start of treatment, mice were euthanized. Coronal sections of mouse tumors were fixed in 10% buffered formalin, paraffin-embedded, and cut into 3 μm thick sections. These sections were then stained with hematoxylin and eosin for histologic evaluation.

4.18. Immunohistochemical staining

The proliferative activity of tumor cells was evaluated using Ki-67 staining. Tumor tissue sections were incubated with a primary antibody (anti-Ki-67 monoclonal antibody at a concentration of 1 : 200) in a wet box at 4 °C for 12 h. The following day, the sections were washed with PBS and incubated with a horseradish peroxidase (HRP)-labeled secondary antibody at room temperature for 1 h. The DAB color solution was used to develop the staining for 3–5 min, and the degree of staining was controlled under the microscope. Hematoxylin staining of nuclei was repeated for 1 min, and the sections were dehydrated with ethanol, made transparent with xylene, and sealed with neutral gum for microscopic observation.

4.19. Immunofluorescence test

TUNEL staining was used to detect apoptotic cells in tumor tissues. Paraffin-embedded tumor tissue sections were dewaxed, hydrated, and digested with 20 μg mL^{-1} proteinase K solution at 37 °C for 15 min. The TUNEL reaction mixture was applied to the tissue and incubated for 1 h at 37 °C in a wet box protected from light. The tissue was washed with PBS, sealed with an anti-fluorescence quenching sealer, and observed under a fluorescence microscope (Nikon).

Dihydroethidium (DHE) staining was used to detect ROS levels in tumor tissues. Fresh tumor tissue was processed into frozen sections according to standard protocols. The sections were incubated with anti-DHE primary antibody (Beyotime) overnight, washed three times with PBS, and incubated with secondary antibody (Beyotime) at room temperature for 1 h. Nuclei were stained with DAPI, and the sections were examined and imaged under a fluorescence microscope (Nikon).

4.20. Serum biochemistry analysis

At designated time points, the mice were euthanized, and serum samples were collected. All samples were centrifuged at 5000 rpm for 10 minutes. Levels of alkaline phosphatase (ALP), alanine aminotransferase (ALT), aspartate aminotransferase (AST), creatinine (CRE), and blood urea nitrogen (BUN) were measured using an automated Cobas 8000 analyzer (Roche, Germany) equipped with a c702 module.

4.21. Statistical analysis

Statistical analysis of the experimental data was conducted with GraphPad Prism 10. Results are expressed as mean ± standard deviation, and differences between groups were assessed for significance by *t*-test (two groups) or one-way ANOVA (multiple

groups), with significance levels labeled as $*P < 0.05$, $**P < 0.01$, and $***P < 0.001$.

Author contributions

Y. Deng: investigation, methodology, and writing – original draft. X. Fang: methodology and formal analysis. Y. Lv: software and data curation. X. Zhu: validation and investigation. Y. Wang, X. Wang and X. Feng: funding acquisition, supervision and writing – review & editing.

Conflicts of interest

The authors have declared no conflicts of interest.

Abbreviations

AFM	Atomic force microscope
CDT	Chemodynamic therapy
CLSM	Confocal laser scanning microscope
DAPI	Diamidino-2-phenylindole
DCFH-DA	2′,7′-dichlorodihydrofluoresceindiacetate
DCTB	*trans*-2-[3-(4-*tert*-butylphenyl)-2-methyl-2-propenylidene]malononitrile
DDW	Double distilled water
DHE	Dihydroethidium
DLS	Dynamic light scattering
DMEM	Dulbecco's modified Eagle's medium
DMF	*N*,*N*-Dimethylformamide
DMPO	5,5-Dimethyl-1-pyrroline *N*-oxide
DMSO	Dimethyl sulfoxide
DTNB	5,5′-Dithiobis-(2-nitrobenzoic acid)
EPR	Electron paramagnetic resonance
FBS	Fetal bovine serum
FT-IR	Fourier transform infrared
GSH	Glutathione
GSSG	Oxidized glutathione
ICP	Inductively coupled plasma
IMDM	Iscove's modified Dulbecco's medium
MALDI-TOF	Matrix assisted laser desorption ionization time of flight
MOC	Metal organic cage
MRI	Magnetic resonance imaging
NPs	Nanoparticles
PBS	Phosphate buffer saline
PDI	Polymer dispersity index
ROS	Reactive oxygen species
SEC	Size exclusion chromatography
TEM	Transmission electron microscope
THF	Tetrahydrofuran
TMB	3,3′,5,5′-Tetramethylbenzidine-4,4′-Bi-2,6-xylidine
TME	Tumor microenvironment
WHO	World Health Organization
XPS	X-ray photoelectron spectroscopy

Data availability

The data supporting this article have been included as part of the supplementary information (SI). Supplementary information is available. See DOI: **https://doi.org/10.1039/d5mh01167a**.

Acknowledgements

The authors acknowledge funding from the National Key Research and Development Program of China (2023YFF0724101), the Natural Science Foundation of Shanghai (25ZR1403006), and the Fundamental Research Funds for the Central Universities (YG2023QNA04).

References

1 C. W. Bailey and M. K. Sydnor, *Dig. Dis. Sci.*, 2019, **64**, 951–958.
2 N. A. Cortes-Mejia, H. A. Lillemoe and J. P. Cata, *Curr. Oncol. Rep.*, 2024, **26**, 1420–1430.
3 E. I. Hwang, E. J. Sayour, C. T. Flores, G. Grant, R. Wechsler-Reya, L. B. Hoang-Minh, M. W. Kieran, J. Salcido, R. M. Prins, J. W. Figg, M. Platten, K. M. Candelario, P. G. Hale, J. E. Blatt, L. S. Governale, H. Okada, D. A. Mitchell and I. F. Pollack, *Nat. Cancer*, 2022, **3**, 11–24.
4 S. T. Paijens, A. Vledder, M. de Bruyn and H. W. Nijman, *Cell. Mol. Immunol.*, 2021, **18**, 842–859.
5 X. Chen, Y. Liu and W. Bu, *Sci. Sin.: Chim.*, 2020, **50**, 159–172.
6 D. Sun, X. Sun, X. Zhang, J. Wu, X. Shi, J. Sun, C. Luo, Z. He and S. Zhang, *Adv. Healthcare Mater.*, 2024, **13**, 2400809.
7 P. Zhao, H. Li and W. Bu, *Angew. Chem., Int. Ed.*, 2023, **62**, e202210415.
8 X. Zhu-Ge, D.-M. Xi and S.-S. Zhang, *Chin. J. Anal. Chem.*, 2022, **50**, 100121.
9 J. Cai, Q. Shen, Y. Wu, J. Hu, D. Pan, Y. Wu and B. Geng, *Adv. Funct. Mater.*, 2024, **34**, 2411064.
10 B. Geng, J. Hu, X. He, Z. Zhang, J. Cai, D. Pan and L. Shen, *Adv. Mater.*, 2024, **36**, 2313670.
11 Y. Wang, T. Yan, J. Cai, H. Dou, Y. Zhu, B. Geng, D. Pan and L. Shen, *Biomaterials*, 2025, **321**, 123319.
12 D. A. Fernandes, *Technol. Cancer Res. Treat.*, 2023, DOI: **10.1177/15330338231191493**.
13 N. Parthasarathy, R. Thangam, B. Rithisa, S. Sudhakar, K. Shanthi, H. Hong, M. Sathuvan, M. Fabiola, H. Kang and R. Vivek, *Coord. Chem. Rev.*, 2025, **530**, 216489.
14 J. D. Urbano-Gámez, C. Guzzi, M. Bernal, J. Solivera, I. Martínez-Zubiaurre, C. Caro and M. L. García-Martín, *Int. J. Mol. Sci.*, 2024, **25**, 5213.
15 Shreyas P. Vaidya, S. Gadre, Ravi T. Kamisetti and M. Patra, *Biosci. Rep.*, 2022, **42**, BSR20212160.
16 W. Wang, Z. Huang, Y. Huang, X. Pan and C. Wu, *Int. J. Pharm.*, 2020, **589**, 119815.
17 X. Zhong, X. Dai, Y. Wang, H. Wang, H. Qian and X. Wang, *WIREs Nanomed. Nanobiotechnol.*, 2022, **14**, e1797.
18 C. Jia, Y. Guo and F.-G. Wu, *Small*, 2022, **18**, 2103868.

19 H. Gizem Özkan, V. Thakor, H.-G. Xu, G. Bila, R. Bilyy, D. Bida, M. Böttcher, D. Mougiakakos, R. Tietze and A. Mokhir, *Chem. – Eur. J.*, 2022, **28**, e202104420.
20 G. Taşkor Önel, E. Özgül Karaaslan, İ. Ösken and N. Saygılı, *Chem. Pap.*, 2022, **76**, 2249–2257.
21 G. Zeh, P. Haines, M. E. Miehlich, T. Kienz, A. Neidlinger, R. P. Friedrich, H. G. Özkan, C. Alexiou, F. Hampel, D. M. Guldi, K. Meyer, J. Schatz, K. Heinze and A. Mokhir, *Organometallics*, 2020, **39**, 3112–3120.
22 Y. Chang, K. Yang, P. Wei, S. Huang, Y. Pei, W. Zhao and Z. Pei, *Angew. Chem., Int. Ed.*, 2014, **53**, 13126–13130.
23 Y. Wang, B. Sun, B. Han and M. Hu, *RSC Adv.*, 2018, **8**, 27740–27745.
24 N. Judge, L. Wang, Y. Y. L. Ho and Y. Wang, *Macromol. Res.*, 2018, **26**, 1074–1084.
25 D. Sun, X. Feng, X. Zhu, Y. Wang and J. Yang, *Coord. Chem. Rev.*, 2024, **500**, 215546.
26 Y.-P. Wang, Y. Zhang, X.-H. Duan, J.-J. Mao, M. Pan, J. Shen and C.-Y. Su, *Coord. Chem. Rev.*, 2024, **501**, 215570.
27 C. Huang, Y. Deng, R. Ma, H. Ge, F. Gong, J. Yang, X. Zhu and Y. Wang, *Nanoscale*, 2024, **16**, 9406–9411.
28 W.-Z. Li, X.-F. Rong, Y. Wang, J.-W. Xiong, N. Zhou, Z.-X. Wang, X.-J. Fang, W. Wang, Y. Liu and X.-Q. Wang, *Chem. Eng. J.*, 2024, **491**, 152015.
29 D. Sun, Y. Deng, J. Dong, X. Zhu, J. Yang and Y. Wang, *Chem. Eng. J.*, 2024, **497**, 154648.
30 L. K. Moree, L. A. V. Faulkner and J. D. Crowley, *Chem. Soc. Rev.*, 2024, **53**, 25–46.
31 C. Yu, P. Yang, X. Zhu and Y. Wang, *Sci. China: Chem.*, 2022, **65**, 858–862.
32 C. Huang, Z. Liu, Y. Deng, X. Wang, Q. Miao, D. Sun, X. Zhu, J. Yang and Y. Wang, *Theranostics*, 2025, **15**, 2564–2578.
33 H. Liu, H.-H. Lu, Y. Alp, R. Wu and S. Thayumanavan, *Prog. Polym. Sci.*, 2024, **148**, 101765.
34 Y. Duan, Q. Li, P. He, Y. Li, J. Song, J. Wang, J. Liu, J. Zhou, F. Chen, Z. Huang, J. Sun, Y. Zhang and Z. Luo, *Chin. Chem. Lett.*, 2022, **33**, 3217–3220.
35 L. Qi, H. Ding, C. Lu and X. Wang, *Luminescence*, 2023, **38**, 1167–1174.
36 A. Dasgupta, E. Richards and R. L. Melen, *Angew. Chem., Int. Ed.*, 2021, **60**, 53–65.
37 Y. Ran, M. Moursy, R. C. Hider and A. Cilibrizzi, *Int. J. Mol. Sci.*, 2023, **24**, 4162.
38 G. An, H. Zheng, L. Guo, J. Huang, C. Yang, Z. Bai, N. Wang, W. Yang and Y. Zhu, *J. Colloid Interface Sci.*, 2024, **662**, 298–312.
39 C. Feng, L. Wang, D. Zhang, L. Geng, L. Zhou, L. Wang, G. Tian, Q. Tang, J. Hu, B. Geng and L. Yan, *J. Colloid Interface Sci.*, 2024, **665**, 681–692.
40 Y. Liu, J. Wu, Y. Jin, W. Zhen, Y. Wang, J. Liu, L. Jin, S. Zhang, Y. Zhao, S. Song, Y. Yang and H. Zhang, *Adv. Funct. Mater.*, 2019, **29**, 1904678.
41 L. Wang, Y. Xu, C. Liu, W. Si, W. Wang, Y. Zhang, L. Zhong, X. Dong and Y. Zhao, *Chem. Eng. J.*, 2022, **438**, 135567.
42 Y. Wang, K. Huang, T. Wang, L. Liu, F. Yu, W. Sun, W. Yao, H. Xiong, X. Liu, H. Jiang and X. Wang, *Small*, 2024, **20**, 2310300.
43 J. Yang, L. Yang, Q. Li and L. Zhang, *J. Colloid Interface Sci.*, 2022, **626**, 719–728.
44 K. Zhang, H. Sun, L. Wei, R. Hu, H. Liu, Y. Lai and X. Li, *Spectrochim. Acta, Part A*, 2025, **328**, 125439.
45 Y. Chen, C. J. Miller and T. D. Waite, *Environ. Sci. Technol.*, 2022, **56**, 1278–1288.
46 P. Huang, X. Qian, Y. Chen, L. Yu, H. Lin, L. Wang, Y. Zhu and J. Shi, *J. Am. Chem. Soc.*, 2017, **139**, 1275–1284.
47 R. Qin, S. Li, Y. Qiu, Y. Feng, Y. Liu, D. Ding, L. Xu, X. Ma, W. Sun and H. Chen, *Nat. Commun.*, 2022, **13**, 1938.
48 F. Slade, J. F. Collingwood and N. J. Rogers, *Coord. Chem. Rev.*, 2024, **516**, 215940.
49 W. Zhao, C. Li, J. Chang, H. Zhou, D. Wang, J. Sun, T. Liu, H. Peng, Q. Wang, Y. Li and A. K. Whittaker, *Prog. Polym. Sci.*, 2023, **146**, 101739.
50 P. Yin, D. Sun, Y. Deng, X. Zhu, Y. Wang, J. Yang and X. Feng, *Theranostics*, 2024, **14**, 4861–4873.
51 C. E. Knezevic, M. A. Ness, P. H. T. Tsang, B. J. Tenney and M. A. Marzinke, *Clin. Chim. Acta*, 2020, **510**, 459–465.
52 C. Shuai, C. Lin, C. He, W. Tan, S. Peng and W. Yang, *J. Colloid Interface Sci.*, 2025, **685**, 1131–1142.
53 Q. Tian, L. An, Q. Tian, J. Lin and S. Yang, *Theranostics*, 2020, **10**, 4101–4115.
54 C. Liu, Y. Cao, Y. Cheng, D. Wang, T. Xu, L. Su, X. Zhang and H. Dong, *Nat. Commun.*, 2020, **11**, 1735.
55 Y. Sun, L. Qin, Y. Yang, J. Gao, Y. Zhang, H. Wang, Q. Wu, B. Xu and H. Liu, *Small*, 2024, **20**, 2402320.
56 S. Zhou, J. Xu, Y. Dai, Y. Wei, L. Chen, W. Feng, Y. Chen and X. Ni, *Biomater. Res.*, 2022, **26**, 66.